Journal of Science and Technology in Civil Engineering NUCE 2019. 13 (3): 58–72

STATIC ANALYSIS OF PIEZOELECTRIC FUNCTIONALLY GRADED POROUS PLATES REINFORCED BY GRAPHENE PLATELETS

Nguyen Thi Bich Lieu[a,*], Nguyen Xuan Hung[b]

[a]*Ho Chi Minh City University of Technology and Education, No 1 Vo Van Ngan street, Thu Duc district, Ho Chi Minh city, Vietnam*
[b]*CIRTECH Institute, Ho Chi Minh City University of Technology (HUTECH), 475A Dien Bien Phu street, Binh Thanh district, Ho Chi Minh city, Vietnam*

Article history:
Received 07/08/2019, Revised 24/08/2019, Accepted 28/08/2019

Abstract

In this study, for the first time an isogeometric finite element formulation for bending analysis of functionally graded porous (FGP) plates reinforced by graphene platelets (GPLs) embedded in piezoelectric layers is presented. It is named as PFGP-GPLs for a short. The plates are constituted by a core layer, which contains the internal pores and GPLs dispersed in the metal matrix either uniformly or non-uniformly according to three different patterns, and two piezoelectric layers perfectly bonded on the top and bottom surfaces of host plate. The modified Halpin–Tsai micromechanical model is used to estimate the effective mechanical properties which vary continuously along thickness direction of the core layer. In addition, the electric potential is assumed to vary linearly through the thickness for each piezoelectric sublayer. A generalized C^0-type higher-order shear deformation theory (C^0-HSDT) in association with isogeometric analysis (IGA) is investigated. The effects of weight fractions and dispersion patterns of GPLs, the coefficient and distribution types of porosity as well as external electrical voltages on structure's behaviors are investigated through several numerical examples.

Keywords: piezoelectric materials; FG-porous plate; graphene platelet reinforcements; isogeometric analysis.

https://doi.org/10.31814/stce.nuce2019-13(3)-06 © 2019 National University of Civil Engineering

1. Introduction

The porous materials whose excellent properties such as lightweight, excellent energy absorption, heat resistance have been extensively employed in various fields of engineering including aerospace, automotive, biomedical and other areas [1–5]. However, the existence of internal pores leads to a significant reduction in the structural stiffness [6]. In order to overcome this shortcoming, the reinforcement with carbonaceous nanofillers such as carbon nanotubes (CNTs) [7–9] and graphene platelets (GPLs) [10, 11] into the porous materials is an excellent and practical choice to strengthen their mechanical properties.

In recent years, porous materials reinforced by GPLs [12] have been paid much attention to by the researchers due to their superior properties such as lightweight, excellent energy absorption, thermal management [13–15]. The artificial porous materials such as metal foams which possess combinations of both stimulating physical and mechanical properties have been prevalently applied in lightweight structural materials [16, 17] and biomaterials [18]. The GPLs are dispersed in materials

*Corresponding author. *E-mail address:* lieuntb@hcmute.edu.vn (Lieu, N. T. B.)

in order to amend the implementation while the weight of structures can be reduced by porosities [19]. With the combination advantages of both GPLs and porosities, the mechanical properties of the material are significantly recovered but still maintain their potential for lightweight structures [20]. Based on modifying the sizes, the density of the internal pores in different directions, as well as GPL dispersion patterns, the FGP plates reinforced by GPLs (FGP-GPLs) have been introduced to obtain the required mechanical characteristics [21–23]. In the last few years, there have been many studies being conducted to investigate the impacts of GPLs and porosities on the behaviors of structures under various conditions. Based on the Ritz method and Timoshenko beam theory, the authors in Refs. [24, 25] studied the free vibration, elastic buckling and the nonlinear free vibration, post-buckling performances of FGP beams, respectively. The uniaxial, biaxial, shear buckling and free vibration responses of FGP-GPLs were also investigated by [26] based on the first-order shear deformation theory (FSDT) and Chebyshev-Ritz method. Additionally, to investigate the static, free vibration and buckling of FGP-GPLs, [27] utilized IGA based on both FSDT and the third-order shear deformation theory (TSDT).

Piezoelectric material is one of smart material kinds, in which the electrical and mechanical properties have been coupled. One of the key features of the piezoelectric materials is the ability to make the transformation between the electrical power and mechanical power. Accordingly, when a structure embedded in piezoelectric layers is subjected to mechanical loadings, the piezoelectric material can create electricity. On the contrary, the structure can be changed its shape if an electric field is put on. Due to coupling mechanical and electrical properties, the piezoelectric materials have been extensively applied to create smart structures in aerospace, automotive, military, medical and other areas. In the literature of the plate integrated with piezoelectric layers, there are various numerical methods being introduced to predict their behaviors.

In this study, the piezoelectric plate with the core layer composed of FGP materials reinforced by GPLs is considered. Based on concept of sandwich structure, the excellent mechanical properties of structure are created by combining outstanding properties of component materials. Accordingly, the presence of porosities in metal matrix leads to decreasing the weight of structure while the mechanical properties are significantly improved by reinforcing GPLs. Meanwhile, two piezoelectric material layers are embedded on the top and bottom surfaces of a porous core layer.

2. Material properties of a PFGP-GPLs plate

In this study, a sandwich plate with length a, width b and total thickness of $h = h_c + 2h_p$ shown in Fig. 1 is modeled. In which h_c and h_p are the thicknesses of the FGP-GPLs layer, core layer, and the piezoelectric face layers, respectively.

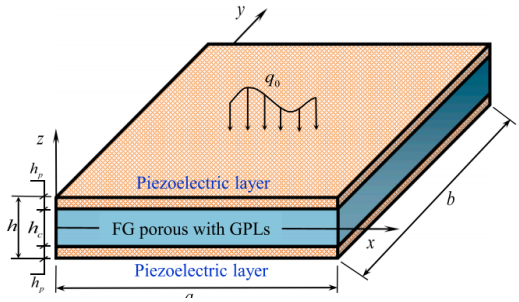
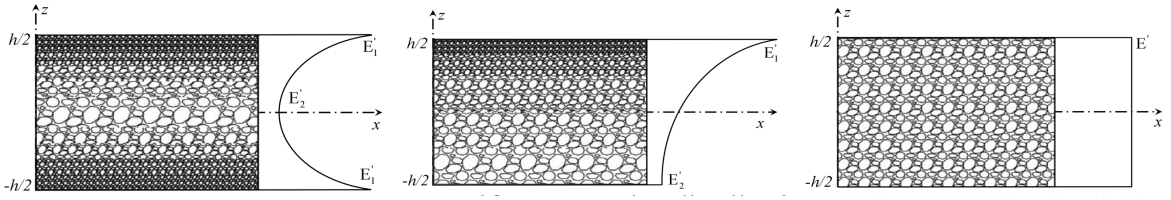


Figure 1. Configuration of a PFGP- GPLs plate

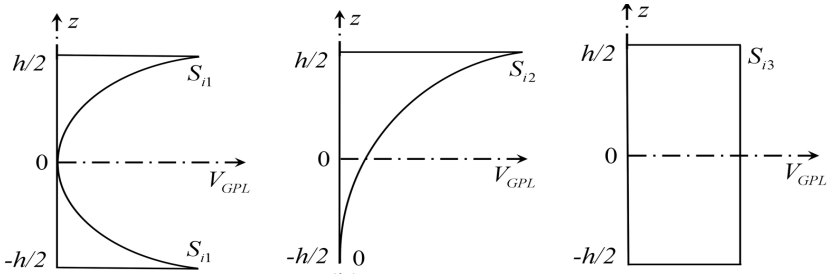
Three different porosity distribution types along the thickness direction of plates including two types of non-uniformly symmetric and a uniform are illustrated in Fig. 2. As presented in this figure, E' is Young's modulus of uniform porosity distribution E'_1 and E'_2 denote the maximum and minimum Young's moduli of the non-uniformly distributed porous material without GPLs, respectively. In addition, three GPL dispersion patterns shown in Fig. 3 are investigated for each porosity

distribution. In each pattern, the GPL volume fraction V_{GPL} is assumed to vary smoothly along the thickness direction.



(a) Non-uniform porosity distribution 1 (b) Non-uniform porosity distribution 2 (c) Uniform porosity distribution

Figure 2. Porosity distribution types [24]



(a) Pattern *A* (b) Pattern *B* (c) Pattern *C*

Figure 3. Three dispersion patterns *A*, *B* and *C* of the GPLs for each porosity distribution type

The material properties including Young's moduli $E(z)$, shear modulus $G(z)$ and mass density $\rho(z)$ which alter along the thickness direction for different porosity distribution types can be expressed as

$$\begin{cases} E(z) = E_1\left[1 - e_0\lambda(z)\right], \\ G(z) = E(z)/\left[2(1+\nu(z))\right], \\ \rho(z) = \rho_1\left[1 - e_m\lambda(z)\right], \end{cases} \tag{1}$$

where

$$\lambda(z) = \begin{cases} \cos(\pi z/h_c), & \text{Non-uniform porosity distribution 1} \\ \cos(\pi z/2h_c + \pi/4), & \text{Non-uniform porosity distribution 2} \\ \lambda, & \text{Uniform porosity distribution} \end{cases} \tag{2}$$

in which $E_1 = E_1'$ and $E_1 = E'$ for types of non-uniformly and uniform porosity distribution, respectively. ρ_1 denotes the maximum value of mass density of the porous core. The coefficient of porosity e_0 can be determined by

$$e_0 = 1 - E_2'/E_1' \tag{3}$$

Through Gaussian Random Field (GRF) scheme [28], the mechanical characteristic of closed-cell cellular solids is given as

$$\frac{E(z)}{E_1} = \left(\frac{\rho(z)/\rho_1 + 0.121}{1.121}\right)^{2.3} \text{ for } \left(0.15 < \frac{\rho(z)}{\rho_1} < 1\right) \tag{4}$$

Then, the coefficient of mass density e_m in Eq. (1) is possibly stated as

$$e_m = \frac{1.121\left(1 - \sqrt[2.3]{1 - e_0\lambda(z)}\right)}{\lambda(z)} \tag{5}$$

Also according to the closed-cell GRF scheme [29], Poisson's ratio $\nu(z)$ is derived as

$$\nu(z) = 0.221p' + \nu_1(0.342p'^2 - 1.21p' + 1) \tag{6}$$

where ν_1 represents the Poisson's ratio of the metal matrix without internal pores and p' is given as

$$p' = 1.121\left(1 - \sqrt[2.3]{1 - e_0\lambda(z)}\right) \tag{7}$$

It should be noted that to obtain a meaningful and fair comparison, the mass per unit of surface M of the FGP plates with different porosity distributions is set to be equivalent and can be calculated by

$$M = \int_{-h_c/2}^{h_c/2} \rho(z)dz \tag{8}$$

Then, the coefficient of porosity ψ in Eq. (1) for uniform porosity distribution can be defined as

$$\lambda = \frac{1}{e_0} - \frac{1}{e_0}\left(\frac{M/\rho_1 h + 0.121}{0.121}\right)^{2.3} \tag{9}$$

The volume fraction of GPLs alters along the thickness of the plate for three dispersion patterns depicted in Fig. 3 can be given as

$$V_{GPL} = \begin{cases} S_{i1}\left[1 - \cos(\pi z/h_c)\right], & \text{Pattern A} \\ S_{i2}\left[1 - \cos(\pi z/2h_c + \pi/4)\right], & \text{Pattern B} \\ S_{i3}, & \text{Pattern C} \end{cases} \tag{10}$$

where S_{i1}, S_{i2} and S_{i3} are the maximum values of GPL volume fraction and $i = 1, 2, 3$ corresponds to two non-uniform porosity distributions 1, 2 and the uniform distribution, respectively.

The relationship between the volume fraction V_{GPL} and weight fractions Λ_{GPL} is given by

$$\frac{\Lambda_{GPL}\rho_m}{\Lambda_{GPL}\rho_m + \rho_{GPL} - \Lambda_{GPL}\rho_{GPL}} \int_{-\frac{h_c}{2}}^{\frac{h_c}{2}} [1 - e_m\alpha(z)]dz = \int_{-\frac{h_c}{2}}^{\frac{h_c}{2}} V_{GPL}\left[1 - e_m\alpha(z)\right]dz \tag{11}$$

By the Halpin-Tsai micromechanical model, Young's modulus E_1 is determined as

$$E_1 = \frac{3}{8}\left(\frac{1 + \zeta_L\eta_L V_{GPL}}{1 - \eta_L V_{GPL}}\right)E_m + \frac{5}{8}\left(\frac{1 + \zeta_w\eta_w V_{GPL}}{1 - \eta_w V_{GPL}}\right)E_m \tag{12}$$

in which

$$\zeta_L = \frac{2l_{GPL}}{t_{GPL}}, \quad \zeta_w = \frac{2w_{GPL}}{t_{GPL}}, \quad \eta_L = \frac{(E_{GPL}/E_m) - 1}{(E_{GPL}/E_m) + \zeta_L}, \quad \eta_w = \frac{(E_{GPL}/E_m) - 1}{(E_{GPL}/E_m) + \zeta_w} \tag{13}$$

where w_{GPL}, l_{GPL} and t_{GPL} denote the average width, length and thickness of GPLs, respectively; E_{GPL} and E_m are Young's moduli of GPLs and metal matrix, respectively. Then, we can determine the mass density ρ_1 and Poison's ratio ν_1 of the GPLs reinforced for porous metal matrix according to the rule of mixture as

$$\rho_1 = \rho_{GPL} V_{GPL} + \rho_m V_m \tag{14}$$

$$\nu_1 = \nu_{GPL} V_{GPL} + \nu_m V_m \tag{15}$$

where ρ_{GPL}, ν_{GPL} and V_{GPL} are the mass density, Poisson's ratio and volume fraction of GPLs, respectively; while ρ_m, ν_m and $V_m = 1 - V_{GPL}$ represent the mass density, Poisson's ratio and volume fraction of metal matrix, respectively.

3. Theory and formulation of PFGP-GPLs plate

3.1. The C^0-type higher-order shear deformation theory (C0-type HSDT)

The higher-order shear deformation theory (HSDT) and the classical plate theory (CPT) bear the relationship to derivation transverse displacement also called slope components. In some numerical methods, it is often difficult to enforce boundary conditions for slope components due to the unification of the approximation variables. Therefore, a C^0-type HSDT is rather recommended. Please see Refs. [30, 31] for more details.

3.2. Garlerkin weak forms of PFGP-GPL plates

The linear piezoelectric constitutive equations can be expressed as follow [31]

$$\begin{bmatrix} \boldsymbol{\sigma} \\ \mathbf{D} \end{bmatrix} = \begin{bmatrix} \mathbf{c} & -\mathbf{e}^T \\ \mathbf{e} & \mathbf{g} \end{bmatrix} \begin{bmatrix} \bar{\boldsymbol{\varepsilon}} \\ \mathbf{E} \end{bmatrix} \tag{16}$$

where $\bar{\boldsymbol{\varepsilon}}$ and $\boldsymbol{\sigma}$ are the strain vector and the stress vector, respectively; $\mathbf{c}$ denotes the elastic constant matrix.

$$\mathbf{c} = \begin{bmatrix} \mathbf{A} & \mathbf{B} & \mathbf{L} & \mathbf{0} & \mathbf{0} \\ \mathbf{B} & \mathbf{G} & \mathbf{F} & \mathbf{0} & \mathbf{0} \\ \mathbf{L} & \mathbf{F} & \mathbf{H} & \mathbf{0} & \mathbf{0} \\ \mathbf{0} & \mathbf{0} & \mathbf{0} & \mathbf{A_S} & \mathbf{B_S} \\ \mathbf{0} & \mathbf{0} & \mathbf{0} & \mathbf{B_S} & \mathbf{D_S} \end{bmatrix} \tag{17}$$

where

$$\begin{aligned} (A_{ij}, B_{ij}, G_{ij}, L_{ij}, F_{ij}, H_{ij}) &= \int_{-h/2}^{h/2} (1, z, z^2, f(z), zf(z), f^2(z)) \bar{Q}_{ij}^b \mathrm{d}z \quad i, j = 1, 2, 6 \\ (A_s^{ij}, B_s^{ij}, D_s^{ij}) &= \int_{-h/2}^{h/2} \left[1, f'(z), (f'(z))^2\right] \bar{Q}_{ij}^s \mathrm{d}z \quad i, j = 4, 5 \end{aligned} \tag{18}$$

The electric field vector $\mathbf{E}$, can be defined as

$$\mathbf{E} = -\mathrm{grad}\phi = -\nabla\phi \tag{19}$$

Note that, for the type of piezoelectric materials considered in this work the stress piezoelectric constant matrices **e**, the strain piezoelectric constant matrices **d** and the dielectric constant matrices **g** can be written as follows

$$\mathbf{e}=\begin{bmatrix} 0 & 0 & 0 & 0 & e_{15} \\ 0 & 0 & 0 & e_{15} & 0 \\ e_{31} & e_{32} & e_{33} & 0 & 0 \end{bmatrix};\ \mathbf{d}=\begin{bmatrix} 0 & 0 & 0 & 0 & d_{15} \\ 0 & 0 & 0 & d_{15} & 0 \\ d_{31} & d_{32} & d_{33} & 0 & 0 \end{bmatrix};\mathbf{g}=\begin{bmatrix} p_{11} & 0 & 0 \\ 0 & p_{22} & 0 \\ 0 & 0 & p_{33} \end{bmatrix} \tag{20}$$

3.3. Approximation of mechanical displacement and electric potential field

a. Mechanical displacement field

Based on the NURBS (Non-Uniform Rational Basis functions), the mechanical displacement field of the FGP plate can be approximated as follows

$$u^h(\xi,\eta)=\sum_{A}^{m\times n} R_A^e(\xi,\eta)d_A \tag{21}$$

where $m\times n$ is the number of basis functions. Meanwhile $R_A^e(\xi,\eta)$ denotes a NURBS basis function and $d_A=\begin{bmatrix} u_{0A} & v_{0A} & w_A & \beta_{xA} & \beta_{yA} & \theta_{xA} & \theta_{yA}\end{bmatrix}^T$ is the vector of nodal degrees of freedom associated with control point A.

The in-plane and shear strains can be rewritten as

$$[\boldsymbol{\varepsilon}\ \boldsymbol{\gamma}]^T=\sum_{A=1}^{m\times n}\begin{bmatrix} \mathbf{B}_A^1 & \mathbf{B}_A^2 & \mathbf{B}_A^3 & \mathbf{B}_A^{s_1} & \mathbf{B}_A^{s_2}\end{bmatrix}^T\mathbf{d}_A \tag{22}$$

where

$$\begin{aligned}
\mathbf{B}_A^1&=\begin{bmatrix} R_{A,x} & 0 & 0 & 0 & 0 & 0 & 0 \\ 0 & R_{A,y} & 0 & 0 & 0 & 0 & 0 \\ R_{A,y} & R_{A,x} & 0 & 0 & 0 & 0 & 0 \end{bmatrix},\quad \mathbf{B}_A^2=-\begin{bmatrix} 0 & 0 & 0 & R_{A,x} & 0 & 0 & 0 \\ 0 & 0 & 0 & 0 & R_{A,y} & 0 & 0 \\ 0 & 0 & 0 & R_{A,y} & R_{A,x} & 0 & 0 \end{bmatrix}\\
\mathbf{B}_A^3&=\begin{bmatrix} 0 & 0 & 0 & 0 & 0 & R_{A,x} & 0 \\ 0 & 0 & 0 & 0 & 0 & 0 & R_{A,y} \\ 0 & 0 & 0 & 0 & 0 & R_{A,y} & R_{A,x} \end{bmatrix}\\
\mathbf{B}_A^{s1}&=\begin{bmatrix} 0 & 0 & R_{A,x} & -R_A & 0 & 0 & 0 \\ 0 & 0 & R_{A,y} & 0 & -R_A & 0 & 0 \end{bmatrix},\quad \mathbf{B}_A^{s2}=\begin{bmatrix} 0 & 0 & 0 & 0 & 0 & R_A & 0 \\ 0 & 0 & 0 & 0 & 0 & 0 & R_A \end{bmatrix}
\end{aligned} \tag{23}$$

b. Electric potential field

The electric potential variation is assumed to be linear in each sublayer and is approximated throughout the piezoelectric layer thickness [32].

3.4. Governing equations of motion

The elementary governing equation of motion can be derived in the following form

$$\begin{bmatrix} \mathbf{M}_{uu} & \mathbf{0} \\ \mathbf{0} & \mathbf{0} \end{bmatrix}\begin{bmatrix} \ddot{\mathbf{d}} \\ \ddot{\boldsymbol{\phi}} \end{bmatrix}+\begin{bmatrix} \mathbf{K}_{uu} & \mathbf{K}_{u\phi} \\ \mathbf{K}_{\phi u} & -\mathbf{K}_{\phi\phi} \end{bmatrix}\begin{bmatrix} \mathbf{d} \\ \boldsymbol{\phi} \end{bmatrix}=\begin{bmatrix} \mathbf{f} \\ \mathbf{Q} \end{bmatrix} \tag{24}$$

where

$$\begin{aligned}\mathbf{K}_{uu} &= \int_{\Omega} \mathbf{B}_u^T \mathbf{c} \mathbf{B}_u \mathrm{d}\Omega; \quad \mathbf{K}_{u\phi} = \int_{\Omega} \mathbf{B}_u^T \tilde{\mathbf{e}}^{\mathbf{T}} \mathbf{B}_\phi \mathrm{d}\Omega \\ \mathbf{K}_{\phi\phi} &= \int_{\Omega} \mathbf{B}_\phi^T \mathbf{g} \mathbf{B}_\phi \mathrm{d}\Omega; \quad \mathbf{M}_{uu} = \int_{\Omega} \tilde{\mathbf{N}}^T \mathbf{m} \tilde{\mathbf{N}} \mathrm{d}\Omega; \quad \mathbf{f} = \int_{\Omega} \bar{\mathbf{q}}_{\mathbf{0}} \bar{\mathbf{N}} \mathrm{d}\Omega\end{aligned} \tag{25}$$

with

$$\begin{aligned}&\mathbf{B}_u = [\mathbf{B}^1 \ \mathbf{B}^2 \ \mathbf{B}^3 \ \mathbf{B}^{s1} \ \mathbf{B}^{s2}]^T; \bar{\mathbf{N}} = \begin{bmatrix} 0 & 0 & R_A & 0 & 0 & 0 & 0 \end{bmatrix}; \\ &\tilde{\mathbf{e}} = \begin{bmatrix} \mathbf{e}_m^T & z\mathbf{e}_m^T & f(z)\mathbf{e}_m^T & \mathbf{e}_s^T & f'(z)\mathbf{e}_s^T \end{bmatrix}\end{aligned} \tag{26}$$

and

$$e_m = \begin{bmatrix} 0 & 0 & 0 \\ 0 & 0 & 0 \\ e_{31} & e_{32} & e_{33} \end{bmatrix}; \quad e_s = \begin{bmatrix} 0 & e_{15} \\ e_{15} & 0 \\ 0 & 0 \end{bmatrix} \tag{27}$$

The global mass matrix $\mathbf{M}_{uu}$ is described as

$$\mathbf{M}_{uu} = \int_{\Omega} \left\{ \begin{Bmatrix} \mathbf{N}_0 \\ \mathbf{N}_1 \\ \mathbf{N}_2 \end{Bmatrix}^T \begin{bmatrix} \mathbf{I}_1 & \mathbf{I}_2 & \mathbf{I}_4 \\ \mathbf{I}_2 & \mathbf{I}_3 & \mathbf{I}_5 \\ \mathbf{I}_4 & \mathbf{I}_5 & \mathbf{I}_6 \end{bmatrix} \begin{Bmatrix} \mathbf{N}_0 \\ \mathbf{N}_1 \\ \mathbf{N}_2 \end{Bmatrix} \right\} \mathrm{d}\Omega \tag{28}$$

where

$$\begin{aligned}\mathbf{N}_0 &= \begin{bmatrix} R_A & 0 & 0 & 0 & 0 & 0 & 0 \\ 0 & R_A & 0 & 0 & 0 & 0 & 0 \\ 0 & 0 & R_A & 0 & 0 & 0 & 0 \end{bmatrix} \\ \mathbf{N}_1 &= -\begin{bmatrix} 0 & 0 & 0 & R_A & 0 & 0 & 0 \\ 0 & 0 & 0 & 0 & R_A & 0 & 0 \\ 0 & 0 & 0 & 0 & 0 & 0 & 0 \end{bmatrix}; \quad \mathbf{N}_2 = \begin{bmatrix} 0 & 0 & 0 & 0 & 0 & R_A & 0 \\ 0 & 0 & 0 & 0 & 0 & 0 & R_A \\ 0 & 0 & 0 & 0 & 0 & 0 & 0 \end{bmatrix}\end{aligned} \tag{29}$$

4. Numerical results

4.1. Convergence and verification studies

In this section, the accuracy and reliability of the proposed method are verified through a numerical example which has just been reported by [33]. The free vibration analysis for a square sandwich FGP-GPLs with simply supported boundary condition (SSSS) is considered. That means the right side of Eq. (24) is zeros vector. The initial parameters of plate are given as: $a = b = 1$ m, $h = 0.005a$, $h_p = 0.1h$, $h_p = 0.8h$, $e_0 = 0.5$. The sandwich plate includes isotropic metal face layers (Aluminum) and a porous core layer which is constituted by the uniformly distributed porous reinforced with uniformly distributed GPLs along the thickness. In this example, the copper is chosen as the metal matrix of the core layer whose material properties, as well as metal face ones, are given Table 1. For the GPLs, the parameters are used as follows: $l_{GPL} = 2.5$ µm, $w_{GPL} = 1.5$ µm, $t_{GPL} = 1.5$ nm and $\Lambda_{GPL} = 1.0wt.\%$.

The convergence and accuracy of present formulation using quadratic ($p = 2$) elements at mesh levels of $7 \times 7, 11 \times 11, 15 \times 15, 17 \times 17$ and 19×19 elements are studied. The natural frequencies generated from the proposed method are compared with analytical solutions [33] based on CPT. Table 2 lists the natural frequencies of the first four m and n values with differentcontrol mesh. Noted that mode 1, mode 5, mode 11 and mode 21 of the vibration correspond with $mn = 1, nm = 1, mn = 13, nm = 31, mn = 3, nm = 3$ and $mn = 3, nm = 5$. These modes are carefully chosen because of

Table 1. Material properties

Properties	Core	Piezoelectric					
	Ti-6Al-4V	Alumium oxide	Al	Al_2O_3	Cu	GPL	PZT-G1195N
Elastic properties							
E11 (GPa)	105.70	320.24	70	380	130	1010	63.0
E22 (GPa)	105.70	320.24	70	380	130	1010	63.0
E33 (GPa)	105.70	320.24	70	380	130	1010	63.0
G12 (GPa)	-	-	-	-	-	-	24.2
G13 (GPa)	-	-	-	-	-	-	24.2
G23 (GPa)	-	-	-	-	-	-	24.2
ν_{12}	0.2981	0.26	0.3	0.3	0.34	0.186	0.30
ν_{13}	0.2981	0.26	0.3	0.3	0.34	0.186	0.30
ν_{23}	0.2981	0.26	0.3	0.3	0.34	0.186	0.30
Mass density							
p (kg/m^3)	4429	3750	2702	3800	8960	1062.5	7600
Piezoelectric coefficients							
d_{31} (m/V)	-	-	-	-	-	-	254×10^{-12}
d_{32} (m/V)	-	-	-	-	-	-	254×10^{-12}
Electric permittivity							
p_{11} (F/m)	-	-	-	-	-	-	15.3×10^{-9}
p_{22} (F/m)	-	-	-	-	-	-	15.3×10^{-9}
p_{33} (F/m)	-	-	-	-	-	-	15.3×10^{-9}

the active vibration in the middle region of the plate where has more damage than other regions [34]. Furthermore, the relative error percentages compared with the analytical solutions are also given in the corresponding column. It can be seen that obtained results from the present approach agree well with the analytical solutions [33] for all selected modes. In addition, Table 2 also reveals that the same accuracy of natural frequency is almost obtained for all modes using quadratic elements at mesh levels of 17×17 and 19×19 elements. The difference between the two mesh levels is not significant. As a result, for a practical point of view, the mesh of 17×17 quadratic elements is applied to model the square plate for all numerical examples.

4.2. Static analysis

In this example, the static analysis of a cantilevered piezoelectric FGM square plate with a size length 400 mm 400 mm is considered. The FGM core layer is made of Ti-6A1-4V and aluminum oxide whose the effective properties mechanical is described based on the rule of mixture [35]. The plate is bonded by two piezoelectric layers which are made of PZT-G1195N on both the upper and lower surfaces symmetrically. The thickness of the FGM core layer is 5 mm and the thickness of each piezoelectric layer is 0.1 mm. All material properties of the core and piezoelectric layers are listed in Table 1. Note that, as power index $n = 0$ implies the FG plate consists only of Ti-6A1-4V while n tends to ∞, the FG plate almost totally consists of aluminum oxide.

Firstly, the effect of input electric voltages on the deflection of the cantilevered piezoelectric FGM square plate subjected to a uniformly distributed load of 100 N/m^2 is examined. Table 3 shows the tip node deflection of FG plate corresponding to various input electric voltages. These results agree well with the reference solutions [36] for all cases. In addition, the centerline deflection of

Table 2. Comparison of convergence of the natural frequency (rad/s) for a square sandwich simply supported FGP-GPLs with different control meshes

Mesh	Methods			
	Mode type (m,n)	Present	Analytical [33]	Relative error* (%)
7×7	(1,1)	161.1793	160.6964	+0.30050
	(1,3)	854.1663	803.4820	+6.30808
	(3,3)	1540.2424	1446.2676	+6.49774
	(3,5)	2885.6399	2731.8389	+5.62994
11×11	(1,1)	160.7703	160.6964	+0.04598
	(1,3)	822.1301	803.4820	+2.32091
	(3,3)	1466.4552	1446.2676	+1.39584
	(3,5)	2799.8612	2731.8389	+2.48998
15×15	(1,1)	160.7038	160.6964	+0.00460
	(1,3)	812.5604	803.4820	+1.12988
	(3,3)	1455.3742	1446.2676	+0.62964
	(3,5)	2766.2133	2731.8389	+1.25828
17×17	(1,1)	160.7008	160.6964	+0.00273
	(1,3)	810.1388	803.4820	+0.82849
	(3,3)	1452.6178	1446.2676	+0.43907
	(3,5)	2755.0973	2731.8389	+0.85138
19×19	(1,1)	160.6970	160.6964	+0.00037
	(1,3)	810.1320	803.4820	+0.82764
	(3,3)	1452.6037	1446.2676	+0.43810
	(3,5)	2755.0870	2731.8389	+0.85100

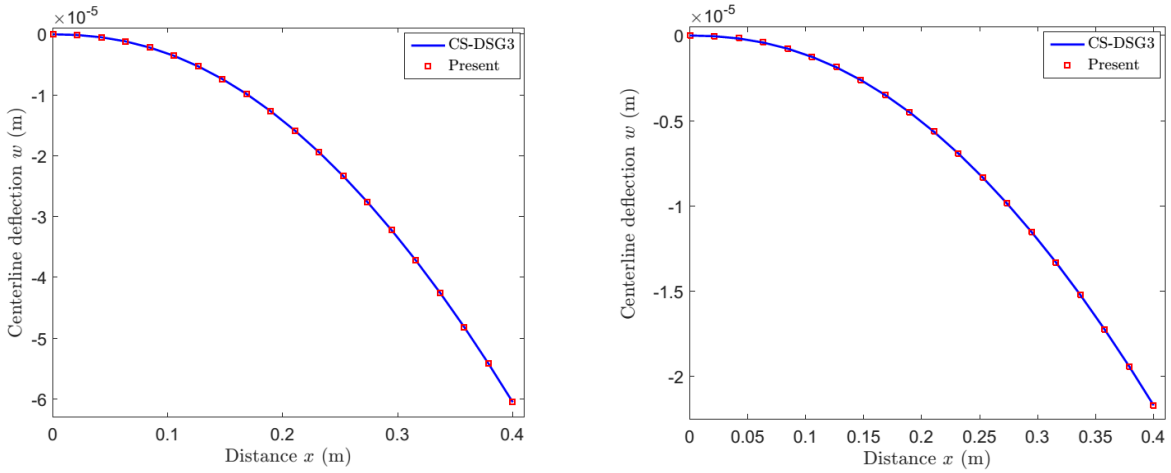
*Relative error $= \dfrac{\text{Present value} - \text{Analytical value}}{\text{Analytical value}} \times 100\%$

piezoelectric FGM square plate only subjected to input electric voltage of 10 V is displayed in Fig. 4. As expected, the obtained results are in good agreement with the reference solution, which is reported by [36]. For further illustration, the centerline deflection of piezoelectric FGM square plate subjected to simultaneously electro-mechanical load is shown in Fig. 5. The observation indicates that when

Table 3. Tip node deflection of the cantilevered piezoelectric FGM plate subjected to a uniform load and different input voltages (10^{-3} m)

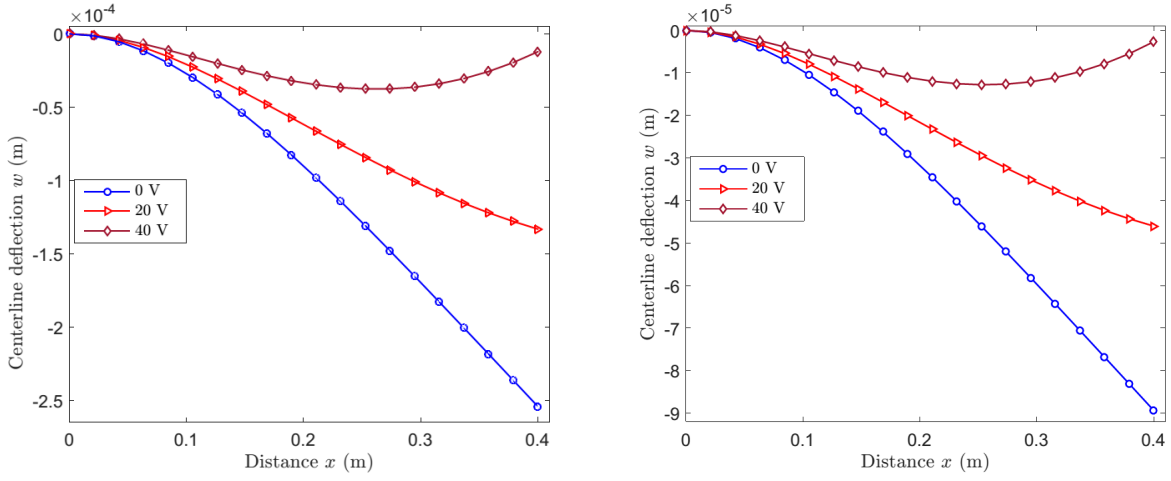
Input voltages (V)	Ti-6Al-4V		Aluminum oxide	
	Present	CS-DSG3 [36]	Present	CS-DSG3 [36]
0	−0.25437	−0.25460	−0.08946	−0.08947
20	−0.13328	−0.13346	−0.04608	−0.04609
40	−0.01229	−0.01232	−0.00271	−0.00271

the input voltage increases, the deflection of the plate becomes smaller because the piezoelectric effect makes the displacement of FGM plate going upward. For the input electric voltage of 40 V, the profile of deflection of the plate is different from those with other electric voltages due to the electric field vector **E** generates the electric field force. This electric field force is opposite to the mechanical force. Therefore, with the same mechanical loading the bigger of the input voltage make the smaller of displacement. However, it should be limitted the value of the input voltage in order to restrict the demolition of structures.



(a) Ti-6Al-4V (b) Aluminum oxide

Figure 4. Profile of the centerline deflection of square piezoelectric FGM plate subjected to input voltage of 10V



(a) Ti-6Al-4V (b) Aluminum oxide

Figure 5. Profile of the centerline deflection of square piezoelectric FGM plate under a uniform loading and different input voltages

Secondly, an FGP-GPLs integrated with piezoelectric layers, PFGP-GPLs, which has the same geometrical dimensions, boundary conditions and pressure loading with above example is investigated. The material properties of porous core and face layers, as well as GPL dimensions, are given

as the same in Section 4.1. Table 4 presents the deflection of tip node of cantilever PFGP-GPLs plate with $\Lambda_{GPL} = 0$ and various porosity coefficients under a uniform loading and different input electric voltages. Through our observation, at a specific of input electrical voltage, an increase in porosity coefficients leads to increasing in the deflection of PFGP-GPL plate because the stiffness of plate will decrease significantly as the higher density and larger size of internal pores. Conversely, the deflection of PFGP-GPL plate decreases when the input voltage increases. Meanwhile, Table 5 shows the tip node deflection of a cantilever PFGP-GPL plate for three GPL dispersion patterns with $\Lambda_{GPL} = 1.0wt.\%$ and $e_0 = 0.2$ under a uniform loading and different input electric voltages. As expected, the effective stiffness of PFGP-GPLs plate can be greatly reinforced after adding a number of GPLs into matrix materials.

Table 4. Tip node deflection $w.10^{-3}$ (m) of a cantilever PFGP-GPLs plate for various porosity coefficients with $\Lambda_{GPL} = 0$ under a uniform loading and different input voltages

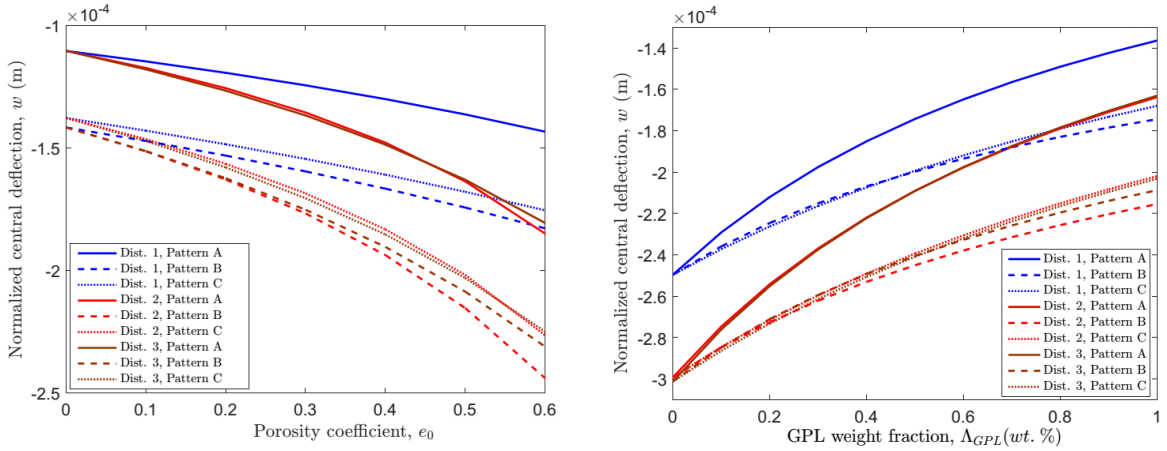
Input voltages (V)	e_0				
	0.0	0.1	0.2	0.4	0.6
	Non-uniform porosity 1				
0	−0.2055	−0.2131	−0.2213	−0.2395	−0.2606
20	−0.1096	−0.1136	−0.1178	−0.1271	−0.1381
40	−0.0137	−0.0140	−0.0142	−0.0148	−0.0156
	Non-uniform porosity 2				
0	−0.2055	−0.2182	−0.2330	−0.2721	−0.3348
20	−0.1096	−0.1162	−0.1238	−0.1438	−0.1761
40	−0.0137	−0.0141	−0.0145	−0.0155	−0.0174
	Uniform porosity				
0	−0.2055	−0.2193	−0.2352	−0.2558	−0.3332
20	−0.1096	−0.1167	−0.1248	−0.1453	−0.1750
40	−0.0137	−0.0141	−0.0144	−0.0154	−0.0168

The careful observation shows that the dispersion pattern *A* dispersed GPLs symmetric through the midplane of plate provides the smallest deflection while the asymmetric dispersion pattern *B* has the largest deflection. As a result, the dispersion pattern *A* yields the best reinforcing performance for the static analysis of PFGP-GPLs plate. Besides, for any specific weight fractions, the GPLs dispersion patterns, input electric voltages and porosity coefficients, the porosity distribution 1 always provides the best reinforced performance as evidenced by obtaining the smallest deflection. This comment is clearly shown in Fig. 6 which shows the effect of porosity coefficients and GPL weight fractions on the tip deflection of PFGP-GPL plates with input electric voltage of 0 V. Possibly to see that the combination between the porosity distribution 1 and GPL dispersion pattern *A* makes the best structural performance for FGP square plate compared with all considered combinations.

Fig. 7 shows the profile of the centerline deflection of the cantilever PFGP-GPLs plate for various core types and input electric voltages under electro-mechanic loading. Accordingly, four core types constituted by the porosity distribution type 1, the GPL dispersion pattern *A* and two values of the

Table 5. Tip node deflection $w.10^{-3}$ (m) of a cantilever PFGP-GPLs plate for three GPL patterns with $\Lambda_{GPL} = 1.0wt.\%$ and $e_0 = 0.2$ under a uniform loading and different input voltages

GPL patterns	Input voltages (V)			
	0	20	40	60
		Non-uniform porosity 1		
A	−1.1938	−0.6299	−0.0664	0.4971
B	−1.5325	−0.8107	−0.0898	0.6311
C	−1.4852	−0.7867	−0.0879	0.6108
		Non-uniform porosity 2		
A	−1.2567	−0.6616	−0.0670	0.5276
B	−1.6308	−0.8607	−0.0917	0.6772
C	−1.5657	−0.8274	−0.0894	0.6486
		Uniform porosity		
A	−1.2666	−0.6667	−0.0669	0.5328
B	−1.6243	−0.8576	−0.0911	0.6754
C	−1.5801	−0.8348	−0.0895	0.6559



(a) Effect of porosity coefficients with $\Lambda_{GPL} = 1.0wt.\%$

(b) Effect of GPL weight fractions with $e_0 = 0.5$

Figure 6. Effect of porosity coefficients and GPL weight fractions on deflection of PFGP-GPL plates with input voltage of 0V

porosity coefficients and weight fraction of GPLs are considered in this example. It is observed that the stiffness of the plate is significantly improved when reinforced by GPLs. Besides, the centreline deflection of the plate tends to go backward to the input electric voltage due to the piezoelectric effect. Therefore, if the porous core layer of plate reinforced by GPLs combines with the piezoelectric material, the displacements of the structure will significantly decrease.

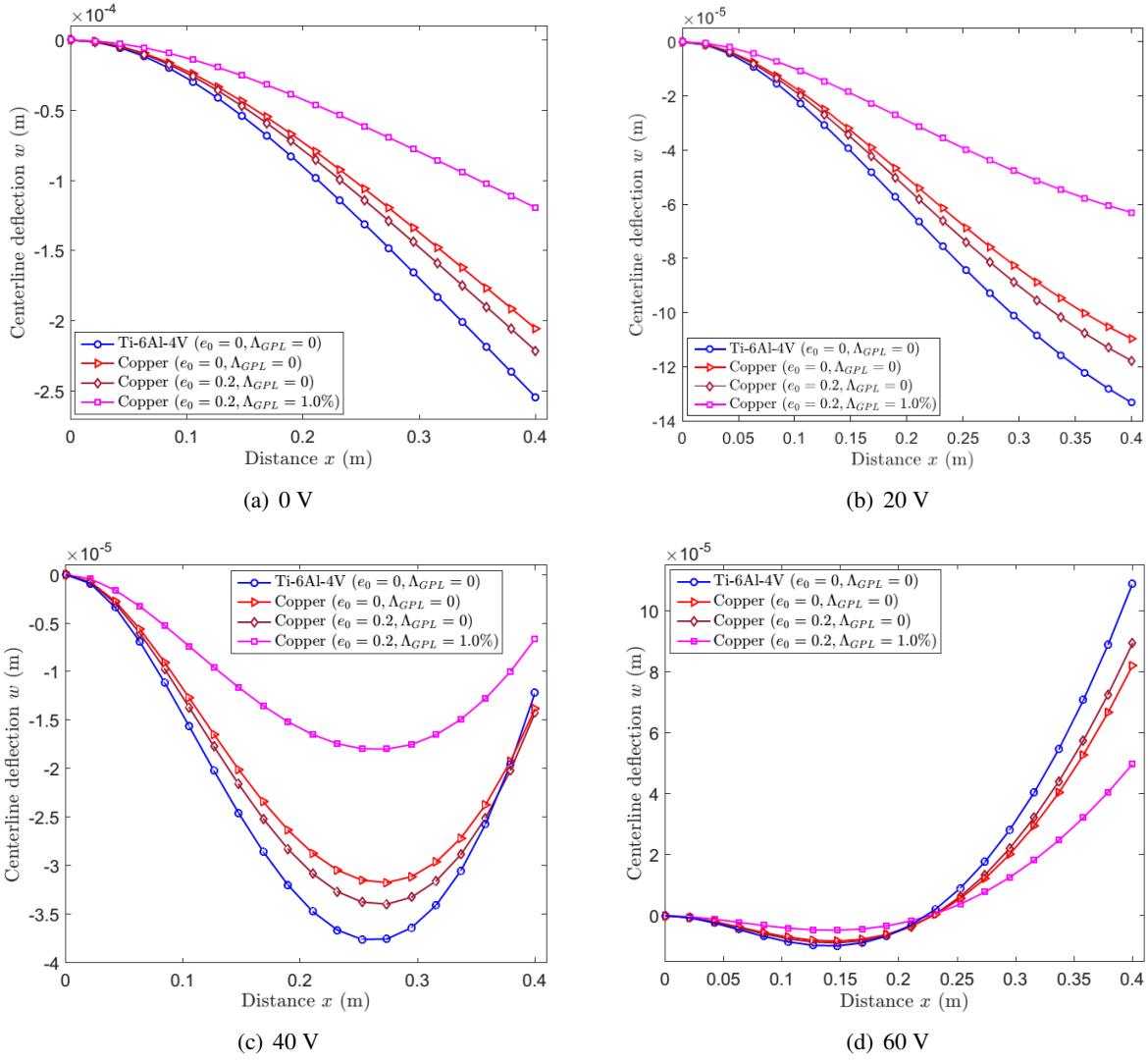


Figure 7. Profile of the centerline deflection of a cantilever PFGP-GPLs plate with many kinds of cores under a uniform loading and different input voltages

5. Conclusions

An effective numerical model within the framework of IGA in associated with the C^0-HSDT has been proposed for the bending responses of PFGP-GPLs plates. The core layer of plate constituted by the combination of three porosity distribution types and dispersion pattern of GPLs, respectively is considered. The mechanical displacement field is approximated through the C^0-HSDT model applying IGA while the electric potential is assumed to vary linearly along the thickness of each piezoelectric sublayer. By the static analyses, the influences of different parameters including external electric voltages, porosity distribution types, porosity coefficients, dispersion patterns and weight fractions of GPL on the behaviors of PFGP-GPLs plates are exhaustively studied. Interestingly, the obtained results agree well with existing studies or available solutions in the literature. Furthermore, we achieved numerical solutions for PFGP-GPLs, while analytical solutions for them have not been found yet.

References

[1] Tampieri, A., Celotti, G., Sprio, S., Delcogliano, A., Franzese, S. (2001). Porosity-graded hydroxyapatite ceramics to replace natural bone. *Biomaterials*, 22(11):1365–1370.

[2] Pompe, W., Worch, H., Epple, M., Friess, W., Gelinsky, M., Greil, P., Hempel, U., Scharnweber, D., Schulte, K. (2003). Functionally graded materials for biomedical applications. *Materials Science and Engineering: A*, 362(1-2):40–60.

[3] Lefebvre, L.-P., Banhart, J., Dunand, D. C. (2008). Porous metals and metallic foams: current status and recent developments. *Advanced Engineering Materials*, 10(9):775–787.

[4] Betts, C. (2012). Benefits of metal foams and developments in modelling techniques to assess their materials behaviour: a review. *Materials Science and Technology*, 28(2):129–143.

[5] Smith, B. H., Szyniszewski, S., Hajjar, J. F., Schafer, B. W., Arwade, S. R. (2012). Steel foam for structures: A review of applications, manufacturing and material properties. *Journal of Constructional Steel Research*, 71:1–10.

[6] Xia, X. C., Chen, X. W., Zhang, Z., Chen, X., Zhao, W. M., Liao, B., Hur, B. (2013). Effects of porosity and pore size on the compressive properties of closed-cell Mg alloy foam. *Journal of Magnesium and Alloys*, 1(4):330–335.

[7] Iijima, S. (1991). Helical microtubules of graphitic carbon. *Nature*, 354(6348):56.

[8] Liew, K. M., Lei, Z. X., Zhang, L. W. (2015). Mechanical analysis of functionally graded carbon nanotube reinforced composites: a review. *Composite Structures*, 120:90–97.

[9] Thanh, N. V., Khoa, N. D., Tuan, N. D., Tran, P., Duc, N. D. (2017). Nonlinear dynamic response and vibration of functionally graded carbon nanotube-reinforced composite (FG-CNTRC) shear deformable plates with temperature-dependent material properties and surrounded on elastic foundations. *Journal of Thermal Stresses*, 40(10):1254–1274.

[10] Mittal, G., Dhand, V., Rhee, K. Y., Park, S.-J., Lee, W. R. (2015). A review on carbon nanotubes and graphene as fillers in reinforced polymer nanocomposites. *Journal of Industrial and Engineering Chemistry*, 21:11–25.

[11] Papageorgiou, D. G., Kinloch, I. A., Young, R. J. (2017). Mechanical properties of graphene and graphene-based nanocomposites. *Progress in Materials Science*, 90:75–127.

[12] Rafiee, M. A., Rafiee, J., Wang, Z., Song, H., Yu, Z.-Z., Koratkar, N. (2009). Enhanced mechanical properties of nanocomposites at low graphene content. *ACS Nano*, 3(12):3884–3890.

[13] Betts, C. (2012). Benefits of metal foams and developments in modelling techniques to assess their materials behaviour: a review. *Materials Science and Technology*, 28(2):129–143.

[14] Lefebvre, L.-P., Banhart, J., Dunand, D. C. (2008). Porous metals and metallic foams: current status and recent developments. *Advanced Engineering Materials*, 10(9):775–787.

[15] Wadley, H. N. G., Fleck, N. A., Evans, A. G. (2003). Fabrication and structural performance of periodic cellular metal sandwich structures. *Composites Science and Technology*, 63(16):2331–2343.

[16] Banhart, J. (2001). Manufacture, characterisation and application of cellular metals and metal foams. *Progress in Materials Science*, 46(6):559–632.

[17] Smith, B. H., Szyniszewski, S., Hajjar, J. F., Schafer, B. W., Arwade, S. R. (2012). Steel foam for structures: A review of applications, manufacturing and material properties. *Journal of Constructional Steel Research*, 71:1–10.

[18] Pompe, W., Worch, H., Epple, M., Friess, W., Gelinsky, M., Greil, P., Hempel, U., Scharnweber, D., Schulte, K. (2003). Functionally graded materials for biomedical applications. *Materials Science and Engineering: A*, 362(1-2):40–60.

[19] Phuong, N. T. B., Tu, T. M., Phuong, H. T., Van Long, N. (2019). Bending analysis of functionally graded beam with porosities resting on elastic foundation based on neutral surface position. *Journal of Science and Technology in Civil Engineering (STCE)-NUCE*, 13(1):33–45.

[20] Duarte, I., Ventura, E., Olhero, S., Ferreira, J. M. F. (2015). An effective approach to reinforced closed-cell Al-alloy foams with multiwalled carbon nanotubes. *Carbon*, 95:589–600.

[21] Hangai, Y., Saito, K., Utsunomiya, T., Kitahara, S., Kuwazuru, O., Yoshikawa, N. (2013). Compression

properties of Al/Al–Si–Cu alloy functionally graded aluminum foam fabricated by friction stir processing route. *Materials Transactions*, page M2012376.

[22] Hassani, A., Habibolahzadeh, A., Bafti, H. (2012). Production of graded aluminum foams via powder space holder technique. *Materials & Design*, 40:510–515.

[23] He, S.-Y., Zhang, Y., Dai, G., Jiang, J.-Q. (2014). Preparation of density-graded aluminum foam. *Materials Science and Engineering: A*, 618:496–499.

[24] Kitipornchai, S., Chen, D., Yang, J. (2017). Free vibration and elastic buckling of functionally graded porous beams reinforced by graphene platelets. *Materials & Design*, 116:656–665.

[25] Chen, D., Yang, J., Kitipornchai, S. (2017). Nonlinear vibration and postbuckling of functionally graded graphene reinforced porous nanocomposite beams. *Composites Science and Technology*, 142:235–245.

[26] Yang, J., Chen, D., Kitipornchai, S. (2018). Buckling and free vibration analyses of functionally graded graphene reinforced porous nanocomposite plates based on Chebyshev-Ritz method. *Composite Structures*, 193:281–294.

[27] Li, K., Wu, D., Chen, X., Cheng, J., Liu, Z., Gao, W., Liu, M. (2018). Isogeometric analysis of functionally graded porous plates reinforced by graphene platelets. *Composite Structures*, 204:114–130.

[28] Selim, B. A., Zhang, L. W., Liew, K. M. (2016). Active vibration control of FGM plates with piezoelectric layers based on Reddy's higher-order shear deformation theory. *Composite Structures*, 155:118–134.

[29] Roberts, A. P., Garboczi, E. J. (2001). Elastic moduli of model random three-dimensional closed-cell cellular solids. *Acta Materialia*, 49(2):189–197.

[30] Thai, C. H., Ferreira, A. J. M., Rabczuk, T., Nguyen-Xuan, H. (2018). A naturally stabilized nodal integration meshfree formulation for carbon nanotube-reinforced composite plate analysis. *Engineering Analysis with Boundary Elements*, 92:136–155.

[31] Phung-Van, P., Nguyen-Thoi, T., Bui-Xuan, T., Lieu-Xuan, Q. (2015). A cell-based smoothed three-node Mindlin plate element (CS-FEM-MIN3) based on the C0-type higher-order shear deformation for geometrically nonlinear analysis of laminated composite plates. *Computational Materials Science*, 96: 549–558.

[32] Nguyen, L. B., Nguyen, N. V., Thai, C. H., Ferreira, A. M. J., Nguyen-Xuan, H. (2019). An isogeometric Bézier finite element analysis for piezoelectric FG porous plates reinforced by graphene platelets. *Composite Structures*, 214:227–245.

[33] Li, Q., Wu, D., Chen, X., Liu, L., Yu, Y., Gao, W. (2018). Nonlinear vibration and dynamic buckling analyses of sandwich functionally graded porous plate with graphene platelet reinforcement resting on Winkler–Pasternak elastic foundation. *International Journal of Mechanical Sciences*, 148:596–610.

[34] Kudus, S. A., Suzuki, Y., Matsumura, M., Sugiura, K. (2018). Vibration-response due to thickness loss on steel plate excited by resonance frequency. In *IOP Conference Series: Earth and Environmental Science*, volume 140, IOP Publishing, 012–123.

[35] Lam, K., Peng, X., Liu, G., Reddy, J. (1997). A finite-element model for piezoelectric composite laminates. *Smart Materials and Structures*, 6(5):583.

[36] Nguyen-Quang, K., Dang-Trung, H., Ho-Huu, V., Luong-Van, H., Nguyen-Thoi, T. (2017). Analysis and control of FGM plates integrated with piezoelectric sensors and actuators using cell-based smoothed discrete shear gap method (CS-DSG3). *Composite Structures*, 165:115–129.